Pull out of FRP reinforcement from masonry pillars: Experimental and numerical results

Gaia Barbieri, Luigi Biolzi, Massimiliano Bocciarelli *, Sara Cattaneo

Department of Architecture, Built Environment and Construction Engineering – ABC, Politecnico di Milano, Piazza Leonardo da Vinci 32, 20133 Milano, Italy

Received 14 July 2014
Received in revised form 3 October 2014
Accepted 10 October 2014
Available online 20 October 2014

1. Introduction

A significant portion of the world culture heritage buildings is constituted by unreinforced masonry structures. Masonry structures are particularly susceptible to damage from accidental loads such as those generated by seismic events that worldwide continue to highlight the need to strengthen these structures. In the last decades, strengthening techniques based on the use of composite materials have been proposed and applied. Among these, one of the most commonly used technique is represented by FRP strips which can be externally glued on both concrete and masonry structures.

FRP materials present several advantages that allow them to be particularly suitable for civil constructions reparation and rehabilitation: high strength-to-weight ratio, corrosion resistance, durability and versatility. However, some concern exists on the bond between the composite material and the substrate, namely the long-term performance and the uncertainties on the failure modes.

In recent years, several experimental and numerical investigations have been conducted for concrete structure reinforced by composite materials [1–6], but only in the last few years some studies have been carried out with reference to masonry supports [7–17] and in some cases FRP reinforcement was adopted for seismic upgrading of existing structures [18].

In this paper, the problem of the bond strength in a "pull–push" test on six CFRP reinforced masonry specimens with different bond length was examined. Single-lap shear tests initially controlled by the loaded edge displacement and subsequently, at the onset of the debonding process, by a clip gauge mounted at the free end of the reinforcement, are presented. The complete equilibrium path was followed up to complete debonding of the reinforcement from the masonry support. According to what suggested by the Italian recommendation [19], the existence of a minimum anchorage length was established, past which the ultimate load cannot further increase.

The experimental tests were simulated by means of a finite element model, based on a cohesive approach to simulate the debonding and on a Riks procedure to follow the snap back-branch of the response.

According to the cohesive approach the non-linearities are concentrated at the interface, while FRP and substrate are characterized by an elastic behavior. In literature, many theoretical models in terms of shear stress versus interface slip were developed for the case of concrete supports, based on observed experimental behavior of strengthened components. Among these, for instance, the models proposed in [1,4,5] are based on an exponential law, while the model proposed in the Italian recommendation [19] is based on a simple bilinear law. In the case of masonry supports, only few studies concerning the modeling of FRP/masonry interface can be found in literature. For instance, in [8,16] an exponential law, in [14] a trilinear law and in [9,10,13,16,19] a bilinear shear

---

* Corresponding author. Tel.: +39 0223994320; fax: +39 0223994369.
E-mail address: massimiliano.bocciarelli@polimi.it (M. Bocciarelli).

stress–slip laws are suggested, often based on models already proposed for concrete supports.

Other micro-modeling approaches based on homogenization techniques [20] or smeared crack models [21] are applied to infer the non-linear material behavior of brick masonry in the presence of quasi-brittle damage.

In the present analyzed cases, the cohesive law approach was used and the interface material parameters identified by means of a best fitting procedure, which allowed reaching a good agreement between the experimental and numerical results, in terms of ultimate load and pre and post-peak response of the CFRP–masonry joint.

2. Experimental techniques

2.1. Specimens preparation and mechanical properties of the materials

Three prismatic masonry specimens were constituted by three standard bricks, with size 250 × 120 × 55 mm, intersected by two fiber-reinforced cement mortar joints with thickness equal to 20 mm. In relation to the size of the test frame, it was necessary to add in the bottom part of the specimen a brick, joined with a layer of bicomponent epoxy adhesive, so as to increase the height of the specimens to the final size of 250 × 120 × 265 mm.

The mechanical properties of brick and mortar, determined according to [22,23], are reported in Table 1. The tests on mortar specimens were conducted after 90 days of curing, just before the test on masonry pillars.

The material properties of the 0.10 mm thick carbon fiber reinforced polymer (CFRP), externally glued to the substrate by an in situ impregnation with an epoxy resin, were: tensile strength equal to 4.8 GPa, Young modulus equal to 215 GPa with a maximum deformation of 2.2%.

The different reinforcement configurations considered are shown in Fig. 1: strips 50 mm width and 50–100–150 mm bond lengths were tested. The purpose was to determine the influence of the reinforcement geometry on the response of the system, in particular the influence of the bond length, and to support the numerical modeling aimed at capturing the failure mechanisms in a pull out test.

2.2. Experimental setup

The testing system consisted of a closed-loop electromechanical Instron load frame with a maximum capacity of 100 kN (Fig. 2). The main characteristics are as follows:

(i) electromechanical control with a minimum speed of 2 μm/h;
(ii) three control channels, one of which can be external (giving the possibility to choose the feedback signal that allows stable test control);
(iii) closed-loop control with integral and derivative gain (in order to remove the effect of the finite stiffness of the machine).

Table 1
Brick and mortar properties.

	Mortar	Brick
Compressive strength f_c (MPa)	45	14
Tensile strength f_t (MPa)	6.0	1.4
Young modulus E (GPa)	15.0	2.4
Poisson's ratio ν	0.10	0.15

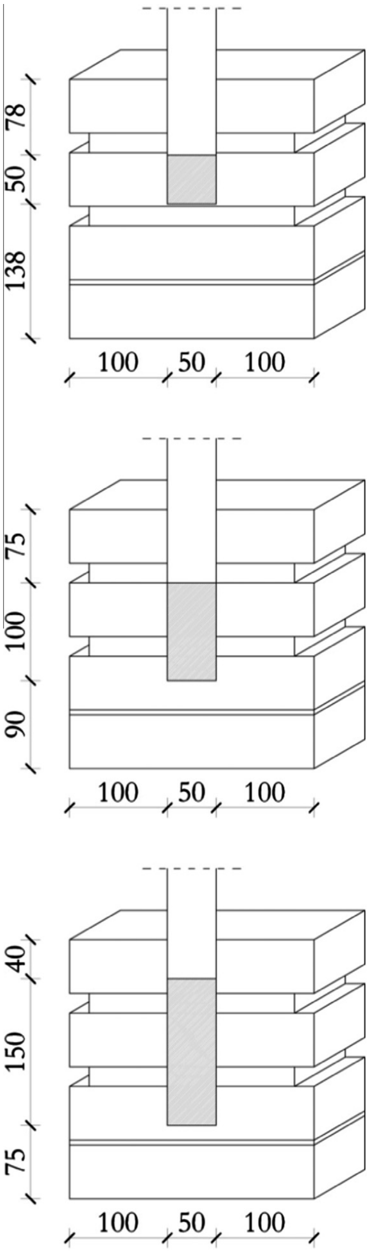

Fig. 1. Configuration of the masonry specimens, values in [mm].

The specimen was fixed by means of a steel support designed to reduce the elastic rotation, i.e. the deformation of the support and of the specimen. The supporting steel plates were controlled by bolts, which permitted reduction in geometrical eccentricities by regulating the specimen arrangement, see Fig. 2. The alignment was checked with an electronic digital caliper with accuracy 0.02 mm. The end of the FRP strip subjected to traction was clamped within two steel plates compressed by bolts. To capture the post-peak behavior of the system even with snap-back softening branch, the tests were performed in a servo-controlled load frame, with a strain gauge transducer (clip gauge), positioned at 10 mm from the free end of the reinforcement, that measured the relative slip between the FRP strip and the substrate, as monotonously increasing feedback signal, see [24]. In addition, two LVDTs measured the relative displacement between the FRP strip at the beginning of the bonded area (at a distance around 25 mm) and the substrate, see Fig. 3.

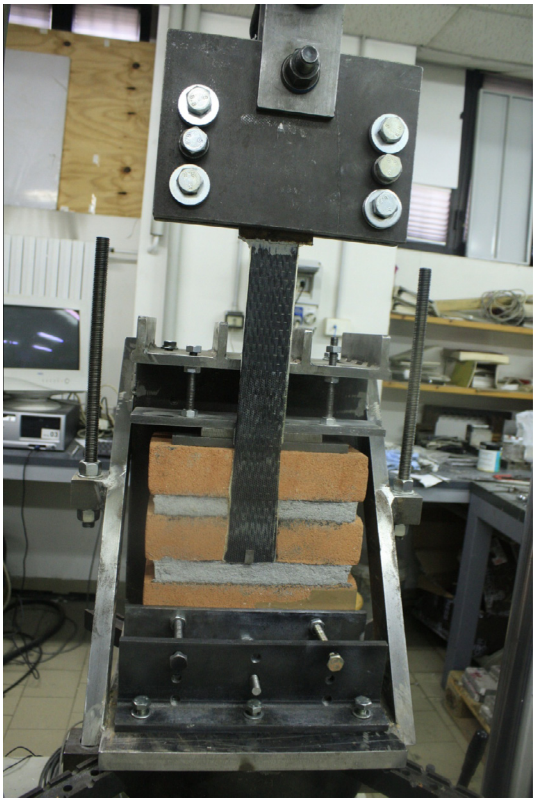

Fig. 2. Test pattern setup for the single shear lap test.

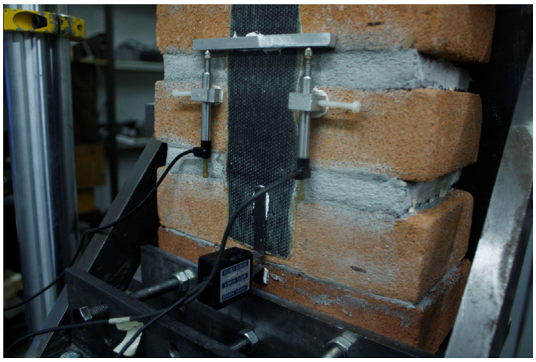

Fig. 3. Point sensors (LVDTs and clip gauge) monitoring relative displacements between the reinforcement and the masonry.

The tests were started in stroke control at a rate of 0.05 μm/s (0.03 μm/s in the case of 150 mm bond length) until the displacement measured by the clip gauge registered some displacements. Then the control was switched to the clip gauge with a speed gradually increasing during the debonding process. So, it was possible to follow stable propagation of fracture.

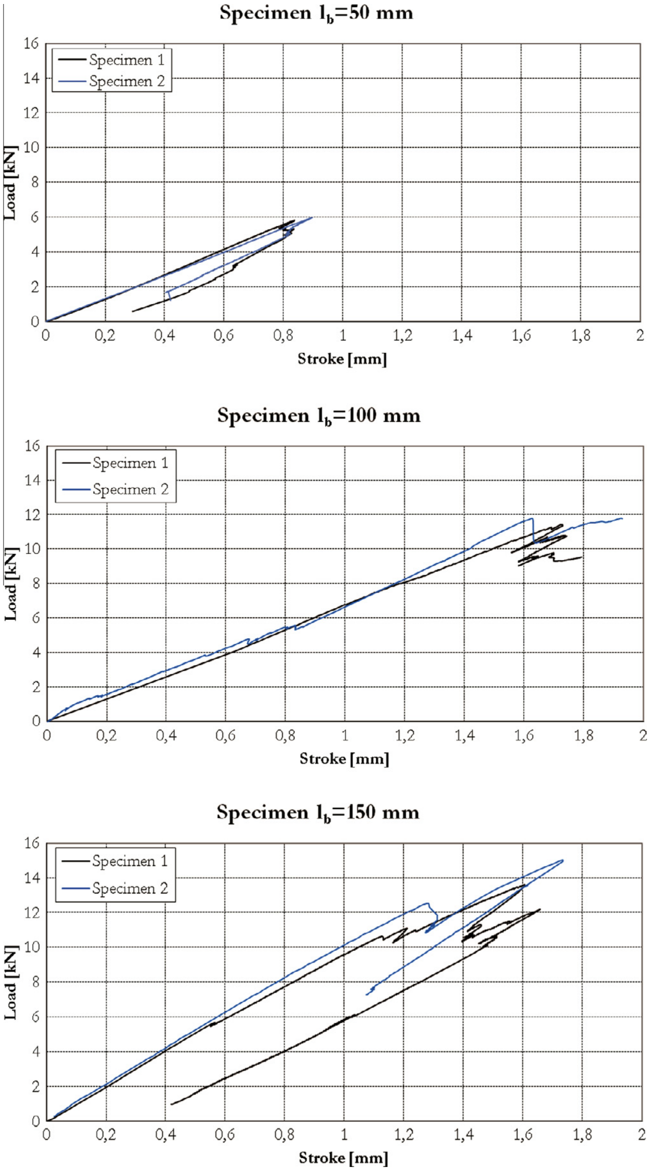

Fig. 4. Load–stroke curves for different bond lengths.

3. Experimental results and comparison with the Italian guidelines

Six specimens were tested, two for each bond length; and the load versus clip gauge displacement curve was measured for one test for each reinforcement length. The brittle response of the joints is shown in Fig. 4. Except for both the tests related to 100 mm bond length, for which the control of the test was lost at the peak load, the load–stroke displacement curves present post-peak snap-back branches, which was possible to follow thanks to the adopted feedback signal. Fig. 5 shows the different load–clip gauge displacement curves for the different bond lengths considered. LVDTs measurements were not considered because strongly affected by a non-uniform propagation of the debonding process, which induced small finite rotations of these instruments.

In Table 2 the results of these experimental tests are summarized and compared to the theoretical predictions based on the design formula suggested in CNR DT200 [19].

According to this recommendation, the specific fracture energy Γ_F and the interface shear strength τ_f can be evaluated as:

$$\begin{cases} \Gamma_F = k_g k_b \sqrt{f_{bc}\, f_{bt}} \\ \tau_f = 2\Gamma_F / s_u \end{cases} \tag{1}$$

where s_u is the maximum interface slip assumed equal to 0.4 mm, k_g is an empirical coefficient (assumed equal to 0.093 mm or 0.031 mm to evaluate the mean Γ_{Fm} or characteristic Γ_{Fk} value, respectively) and k_b is a non-dimensional geometrical coefficient defined as:

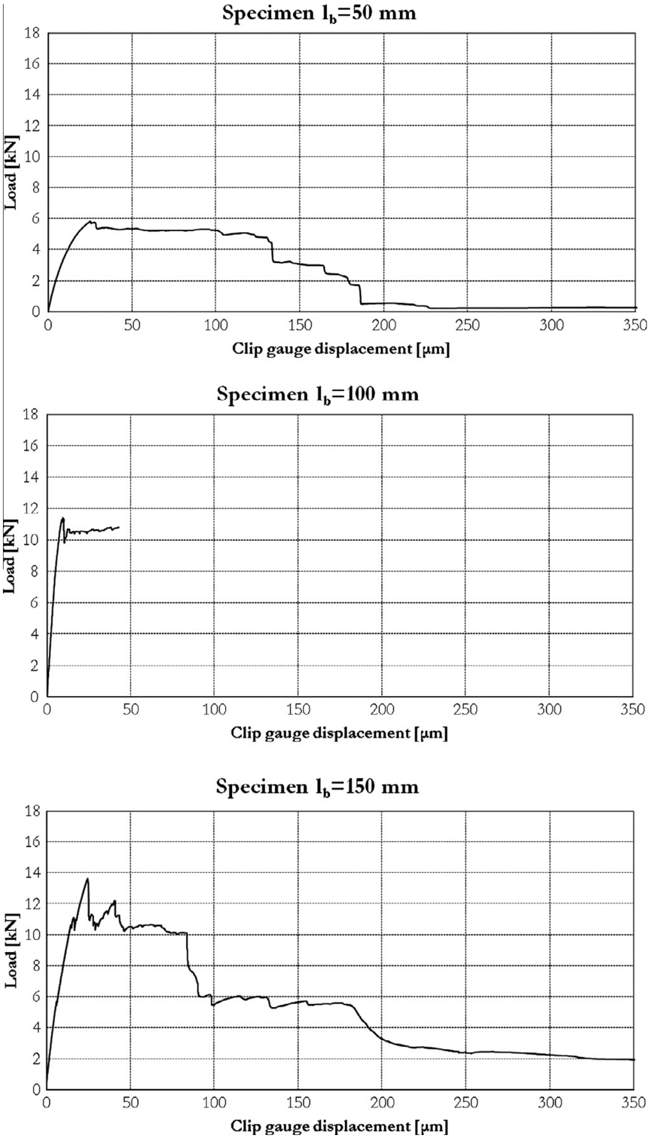

Fig. 5. Load–clip gauge displacement curves for different bond lengths.

$$k_b = \sqrt{\frac{3 - b_f/b}{1 + b_f/b}}, \tag{2}$$

being b_f and b the width of the FRP and of the masonry, respectively. In (1), f_{bc} and f_{bt} denote the mean value of the compressive and tensile strength of the masonry bricks, respectively. The masonry average tensile strength f_{bt} can be assumed equal to 10% of the average compressive strength [19].

According to [19], the minimum bond length l_e is defined as follows:

$$l_e = \frac{1}{\tau_f}\sqrt{\frac{\pi^2 E_f t_f \Gamma_F}{2}}, \tag{3}$$

where τ_f is the interface shear strength, and E_f and t_f are the Young modulus and thickness of FRP strip, respectively. Considering Γ_{Fm} or Γ_{Fk}, the mean bond length l_{em} or the characteristic bond length l_{ek} are assessed, respectively.

According to Eq. (3), the minimum bond length depends on the width of the reinforcement through parameter k_b, used to compute the fracture energy, see Eq. (1), entering the formula for the minimum bond length.

The theoretical maximum force $F_{max,th}$ transmitted by a joint with bond length l_b equal or greater than l_e, is given by:

$$F_{max,th} = b_f\sqrt{2E_f \Gamma_F t_f}, \tag{4}$$

Considering Γ_{Fm} or Γ_{Fk}, the mean maximum force $F_{max,th,m}$ or the characteristic maximum force $F_{max,th,k}$ are computed, respectively.

Conversely, if the effective bond length l_b is smaller than the minimum bond length l_e, the force $F_{max,th}$ has to be reduced to:

$$F_{max,th,rid} = F_{max,th}\frac{l_b}{l_e}\left(2 - \frac{l_b}{l_e}\right). \tag{5}$$

The experimental results confirm that the maximum force increases with the bond length, but once the minimum bond length l_e is guaranteed (Test 2 and 3), the ultimate load cannot further increase significantly and depends on the fracture energy Γ_F only. On the contrary if the minimum bond length l_e is not achieved (Test 1), the maximum force also depends on the reinforcement bond length and, in turns, on the interface shear strength, see Eq. (3).

In the debonding process on strengthened concrete specimens a final competition of two damage mechanisms may occur, see e.g. [25]: (i) debonding along the interface (mode-II), starting from the loaded end and generally affecting few millimeters of the concrete surface, (ii) cracking (mixed-mode) starting at the free end and propagating along an inclined path, with the formation of a resistant bulb. Both debonding and inclined crack opening start when the strain energy release rate, associated with its propagation, is larger than the corresponding fracture energy of the cracked surface. In particular, it turns out that the formation of a resistant bulb allows the system to reach a higher maximum force. This phenomenon affects the load–stroke and load–clip curves with an instantaneous load drop (first peak) corresponding to the formation of the bulb, followed by a new load increase up to failure, see e.g. [25].

In the case of reinforced masonry specimens, the formation of the bulb did not emerge clearly and the delamination seemed to involve the cortical layer of bricks and mortar only (Fig. 6). The mechanical behavior shown in the load–stroke and load–clip curves generally presents a linear (o bilinear) branch up to the maximum load. Only in the case of 150 mm bond length, the curve depicts a first peak before reaching the maximum load. Note that this first peak occurs approximately in correspondence of the maximum load achieved with a 100 mm bond length (around 11.4 kN). Therefore, the formation of the first peak may depict the germinal formation of a bulb, which is also reflected by an increment of the joint performance with respect to the case of bond length equal to 100 mm (see Fig. 4 and Table 2).

Table 2
Comparison in terms of maximum force: experimental and theoretical results.

	Reinforcement	$F_{max,exp}$ (kN)	l_{em} (mm)	l_{ek} (mm)	$F_{max,th,m}$ (kN)	$F_{max,th,k}$ (kN)
Test 1	50 mm × 50 mm	5.8	82	142	7.0	2.8
Test 2	50 mm × 100 mm	11.4	82	142	8.2	4.3
Test 3	50 mm × 150 mm	11.1[a] (13.6[b])	82	142	8.2	4.7

[a] Value of the first peak.
[b] Value of the second peak.

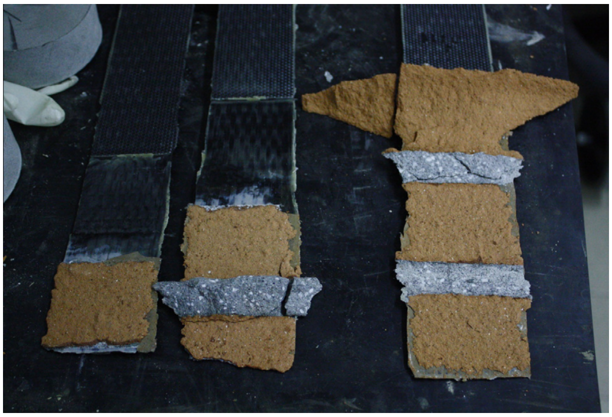

Fig. 6. Failure mechanism for the different bond lengths analyzed.

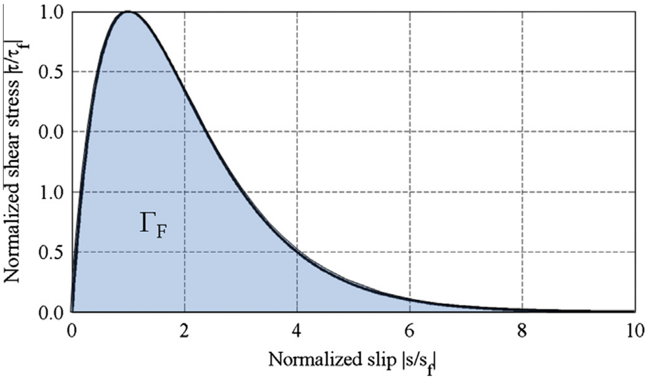

Fig. 8. Exponential bond–slip law adopted in the analyses.

4. Numerical modeling

The push–pull test was simulated adopting a plane stress finite element model implemented in the code Abaqus. The lower edge is constrained in vertical direction and 3/4 of the right edge (starting from the bottom) is constrained in horizontal direction. A displacement is applied to the loaded end of the FRP strip, within a Riks procedure in order to be able to follow the post-failure snap-back branch of the system response. The mesh was refined where higher stress gradients, damage and cracking phenomena were expected. For the models with 50 mm, 100 mm and 150 mm bond lengths, the mesh consisted of 9640, 12,598 and 12,972 linear quadrilateral elements for a total number of 20,382, 26,340, 27,110 DOFs, respectively. Fig. 7 shows the geometry, the constrains and loading conditions of the numerical model, with a zoom in the areas close to the free end of the FRP strip and to the end of the masonry specimen. In particular, zero-thickness interface elements were inserted between masonry substrate and FRP, to take into account the non-linear behavior of the interface, by means of user's defined routine (UEL) implemented in Abaqus and endowed with a proper cohesive law described below. It was assumed that FRP strip, bricks and mortar were linear, elastic materials, with the mechanical properties reported in Section 2.1.

4.1. Cohesive model

Cohesive laws regard fracture as a gradual separation between two surfaces resisted by cohesive tractions which the two surfaces exchange and which are assumed to be function of the opening/sliding displacements.

Several alternative cohesive laws were suggested to describe the interface nonlinear behavior in terms of shear stress versus slip [8]. Bilinear [9,10,13,16] or trilinear [14] cohesive laws are often adopted. However, it is well known that the role played in the numerical simulations by the shape of the cohesive law is marginal compared to the role played by the peak of the curve, i.e. the interface strength, and the area under it, i.e. the fracture energy. In the present analyzed cases, the exponential cohesive law used in [26,27] for steel specimens reinforced using CFRP plates was selected, resuming the one originally proposed in [28].

Assuming w as a scalar measure of the displacement jump vector across the interface, the non-holonomic behavior of the interface model is governed by the maximum attained effective interface jump w_{max}, which represents the only internal variable of the model:

$$w = \sqrt{\beta^2 s^2 + \delta^2}$$
$$\dot{w}_{max} = \begin{cases} \dot{w} & \text{if } w = w_{max} \text{ and } \dot{w} \geqslant 0 \\ 0 & \text{otherwise} \end{cases} \tag{6}$$

where β is a parameter assigning different weights to the sliding, s, and opening, δ, relative displacement components.

Under progressive debonding, the response of the cohesive interface is characterized by a shear stress which increase up to the maximum value τ_f and then it decrease asymptotically to zero in the softening regime, see Fig. 8. Cohesive tractions are obtained by derivatives of the free energy density function φ defined in,

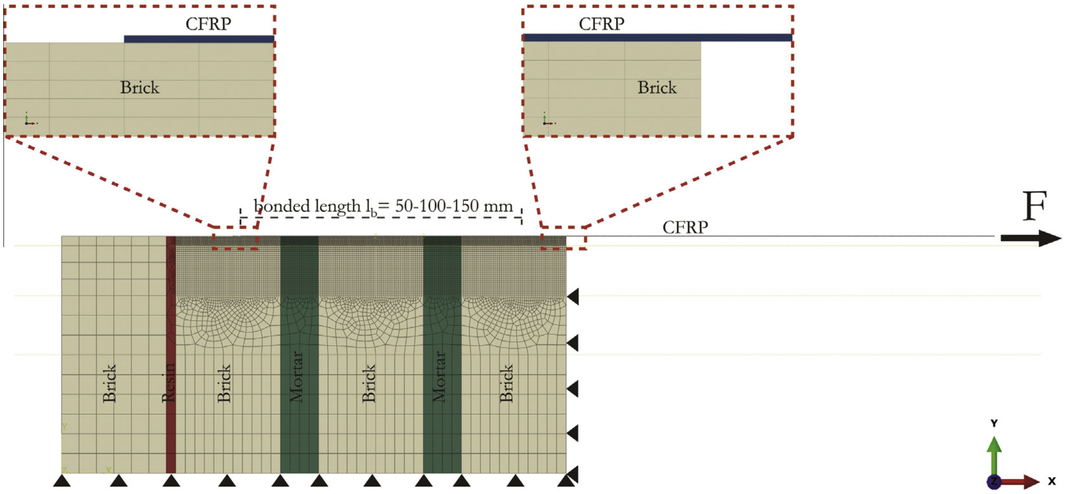

Fig. 7. Geometry, discretization, constraints and loading conditions of the numerical model.

Table 3
Comparison between the parameters τ_f and Γ_{Fm} as suggested by the recommendation [19] and as adopted for the best-fitting curve.

	$\tau_{f,CNR}$ (MPa)	$\tau_{f,bestfit}$ (MPa)	$\frac{\tau_{f,bestfit}}{\tau_{f,CNR}}$	$\Gamma_{Fm,CNR}$ (N/mm)	$\Gamma_{Fm,bestfit}$ (N/mm)	$\frac{\Gamma_{Fm,bestfit}}{\Gamma_{Fm,CNR}}$
Test 1	3.14	2.45	0.78	0.63	0.36	0.57
Test 2	3.14	4.09	1.30	0.63	0.58	0.92
Test 3	3.14	4.09	1.30	0.63	0.58	0.92

e.g., [26], with respect to the relative displacements, while a linear path back to the origin is assumed during unloading, therefore:

$$\begin{cases} \sigma_n = \frac{\partial\varphi}{\partial\delta} = \frac{\sigma_f}{w_c} e^{\left(1-\frac{w}{w_c}\right)}\delta \\ \tau_s = \frac{\partial\varphi}{\partial s} = \frac{\sigma_f}{w_c} e^{\left(1-\frac{w}{w_c}\right)}\beta^2 s \end{cases} \quad \text{if } w = w_{max} \text{ and } \dot{w} \geqslant 0 \tag{7}$$

$$\begin{cases} \sigma_n = \frac{\sigma_f}{w_c} e^{\left(1-\frac{w_{max}}{w_c}\right)}\delta \\ \tau_s = \frac{\sigma_f}{w_c} e^{\left(1-\frac{w_{max}}{w_c}\right)}\beta^2 s \end{cases} \quad \text{if } w < w_{max} \text{ and } \dot{w} < 0 \tag{8}$$

where e is the Neper constant, σ_f is the maximum cohesive normal traction and w_c is a characteristic opening displacement.

The area enclosed by cohesive curves for mode-I and mode-II is the same and represents the fracture energy Γ_F.

Whereas mode-I resistance σ_f and mode-II resistance τ_f, the fracture energy can be defined as follows:

$$\Gamma_F^I = \Gamma_F^{II} = \Gamma_F, \begin{cases} \Gamma_F^I = e\sigma_f w_c \\ \Gamma_F^{II} = e\tau_f w_f \end{cases} \tag{9}$$

where $\tau_f = \beta\sigma_f$ and $w_f = w_c/\beta$.

Therefore, the adopted cohesive law is characterized by three independent parameters: σ_f, τ_f and Γ_F.

As reported in Section 3, in the case of single-lap shear tests, here considered, the delamination process is mode-II dominant, and therefore the adopted mode-dependent cohesive law plays a marginal role.

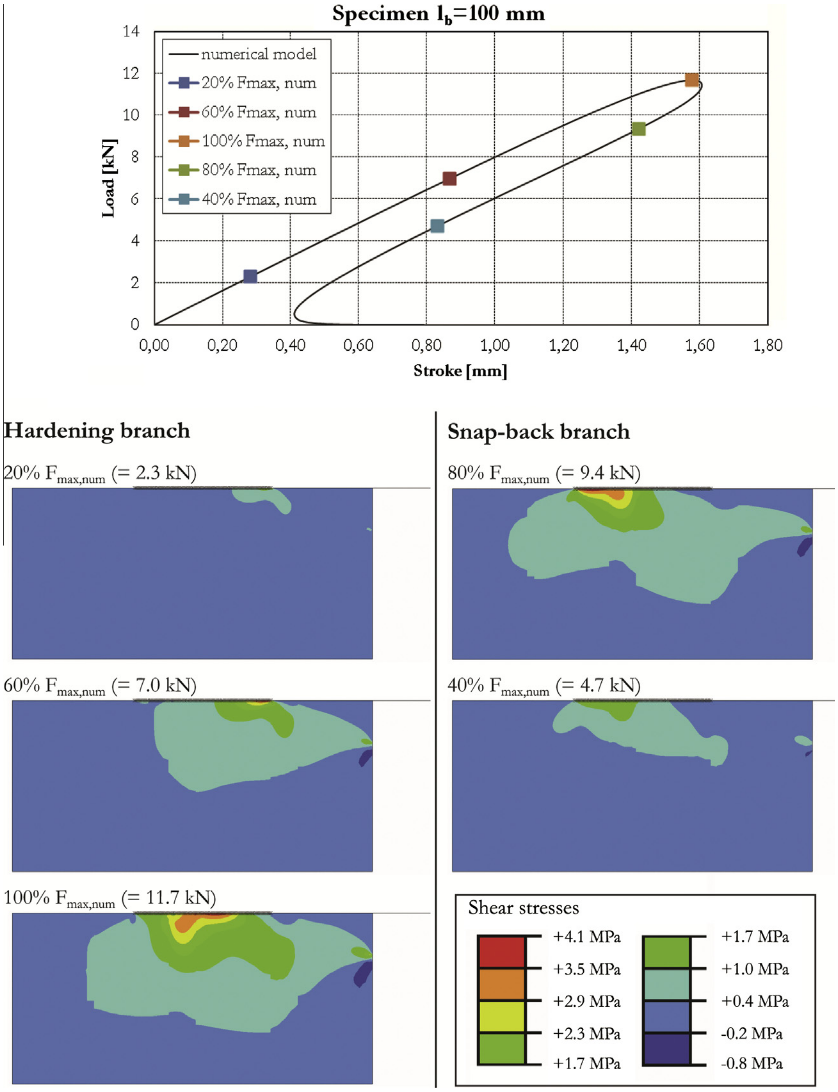

Fig. 9. Shear stress distribution in the support for different load levels. 100 mm bond length.

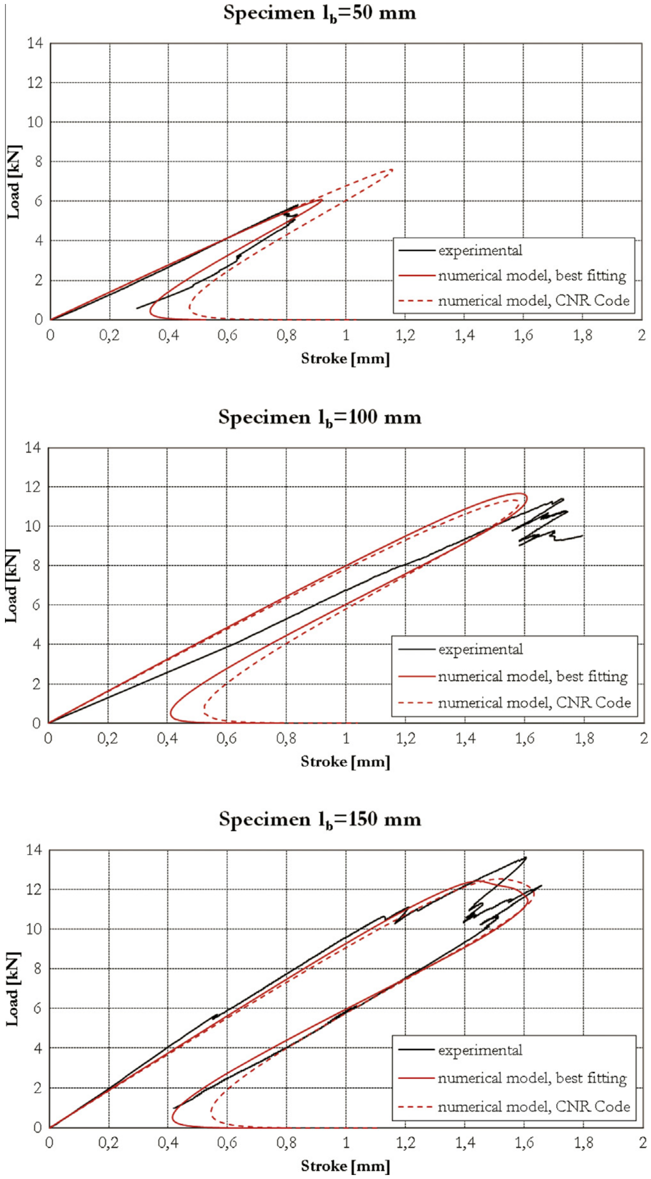

Fig. 10. Comparison between experimental and numerical load–stroke displacement curves for different reinforcement lengths.

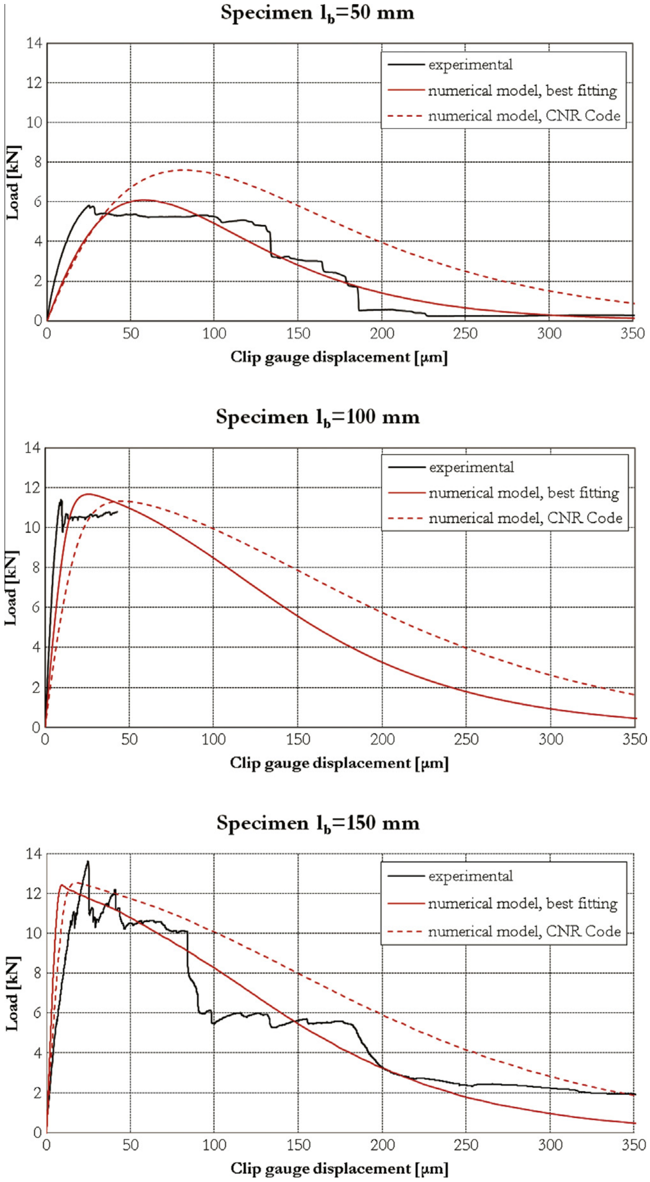

Fig. 11. Comparison between experimental and numerical load–clip gauge displacement curves for different reinforcement lengths.

Table 4
Comparison between experimental and numerical maximum force.

	$F_{max,exp}$ (kN)	$F_{max,num}$ (kN)	Err. (%)
Test 1	5.8	5.9	1.7
Test 2	11.4	11.7	2.6
Test 3	11.1[a] (13.6[b])	12.4	11.7 (−8.8)

[a] Value of the first peak.
[b] Value of the second peak.

5. Comparison between numerical and experimental results

The results of the numerical model were analyzed and compared to the experimental ones, in terms of applied force versus displacement curve and propagation of debonding.

In all cases, the analyses pointed out that debonding starts from the loaded edge of the reinforcement and propagated toward its free end. Such behavior is coherent with the two competing failure mechanisms process observed in the case of strengthened concrete specimens, see [25].

The comparison between the experimental and numerical results was evaluated on the basis of the load–clip gauge displacement curves and the load–stroke displacement curves, the latter being slightly affected by the deformability of the testing system. The comparison was in terms of pre and post-peak response, in view of fact that the implemented model was able to follow also the snap-back branch of the curve.

The numerical results were obtained with a best fitting procedure, changing parameters τ_f and Γ_F starting from those suggested in [19]. Indeed, being the crack failure mode-II dominant, parameter σ_f was non-influent and the only two parameters considered in the inverse analysis were τ_f and Γ_F.

In particular two different interface properties sets were expected and identified, see Table 3: one related to the case of 50 mm bond length, where the interface involves just one brick; and a second one, for the cases of 100 and 150 mm bond length, where the FRP reinforcement is attached to both brick and mortar joint.

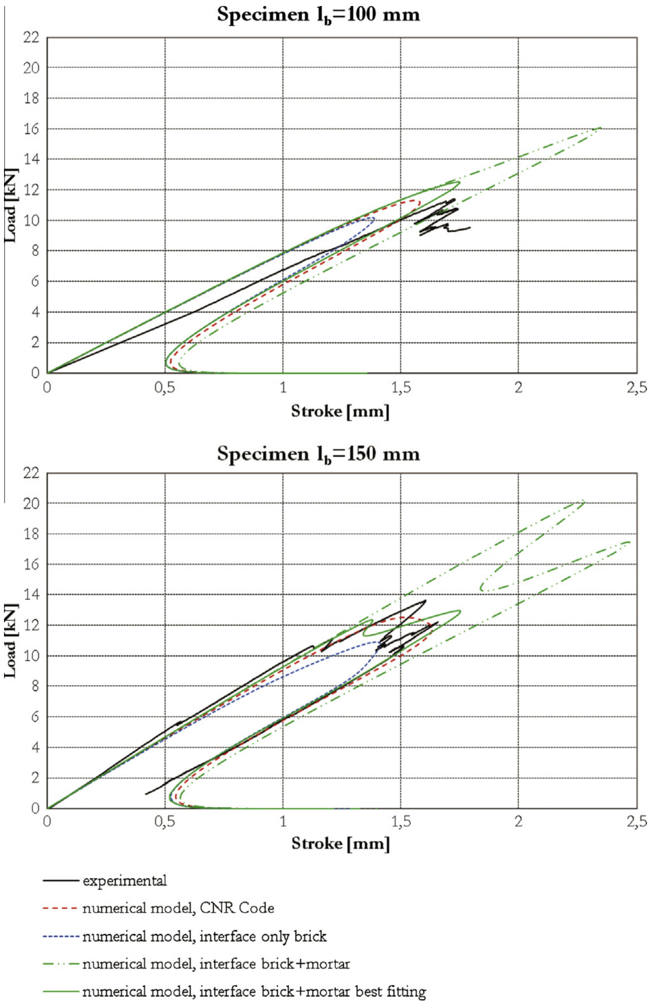

Fig. 12. Parametric numerical analyses and comparison with experimental results, in terms of load–stroke displacement curves, for 100 mm and 150 mm reinforcement lengths.

Fig. 9 visualizes the shear stress distribution in the support for different load levels for the case of 100 mm bond length. It is clearly shown that debonding starts from the loaded edge and propagates toward the free one.

The numerical analyses demonstrated that:

- If $l_b < l_e$ (Test 1), the anchorage length is not long enough to let the cohesive process zone develop completely and therefore the actual load carrying capacity is smaller than the maximum attainable force. $F_{max,th,rid}$ is not only function of the fracture energy Γ_F but also of the interface strength τ_f, see Eqs. (3) and (5). In this case the FEM model endowed with the interface properties, as derived from the CNR guidelines, has a poor predictive capability (Figs. 10 and 11); and the identified values present quite a large difference with respect to the CNR ones (Table 3).
- If $l_b > l_e$ (Test 2 and Test 3), the maximum force is the same as the one attained for $l_b = l_e$. In fact, as soon as the process zone is completely developed, the force cannot increase anymore and $F_{max,th}$ is function of the fracture energy Γ_F only, see Eq.(4). In this case the FEM model endowed with the CNR based interface properties has a good predictive capability (Figs. 10 and 11); and the identified properties values compare well with the CNR ones (Table 3).

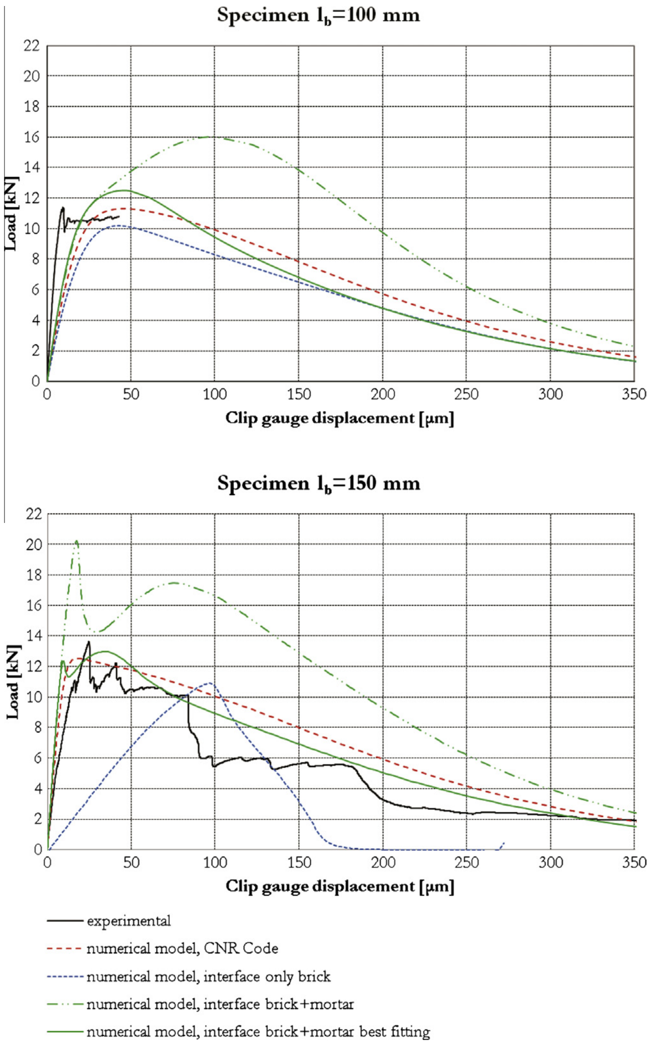

Fig. 13. Parametric numerical analyses and comparison with experimental results, in terms of load–clip gauge displacement curves, for 100 mm and 150 mm reinforcement lengths.

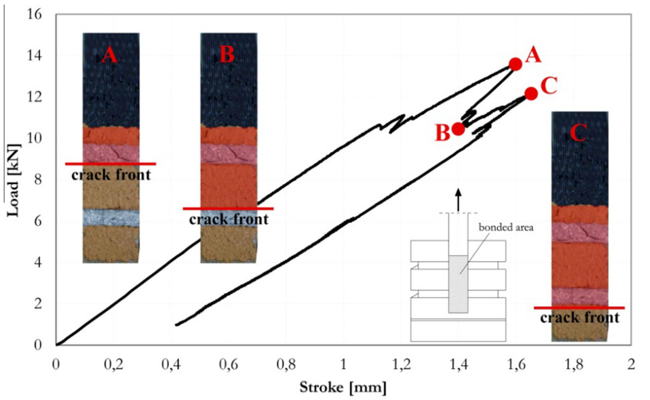

Fig. 14. Main instants of the debonding process and corresponding points in the load displacement curve.

For all specimens tested, the numerical calibration of the parameters Γ_F and τ_f, reported in Table 3, allowed reaching a good agreement between numerical and experimental results, in terms of maximum force, see Table 4, and in terms of overall aspect of the load displacement curves, see Figs. 10 and 11.

In the case of 100 and 150 mm bond length specimens (Test 2 and Test 3) and in relation to the average material properties, the minimum bond length was guaranteed and the maximum force was not affected by the interface strength τ_f. For this reason, this parameter was identified primarily with respect to the experimental stiffness of the systems.

6. Numerical insight on the interface modeling role

Additional numerical cases are here considered in order to better understand the role played by the interface modeling on the overall response of the system. In relation to 100 mm and 150 mm bond lengths, the cases of cohesive law applied on bricks only and on both bricks and mortar layers with different interface properties were investigated.

Interface properties were determined according to Eq. (1), on the basis of the bulk material properties reported in Table 1 (therefore, for brick $\tau_f = 3.14$ MPa and $\Gamma_{Fm} = 0.63$ N/mm; for mortar $\tau_f = 11.67$ MPa and $\Gamma_{Fm} = 2.33$ N/mm).

From Figs. 12 and 13, which depict the response of the specimen with respect to the above defined numerical cases, the following remarks hold:

- If the cohesive law is applied on bricks only (blue dot line) the curve reached a maximum load slightly smaller than the one achieved with the cohesive law applied along the whole interface (red dot line). The role, on the maximum load and the minimum bond length, played by the interface elements, applied on the mortar layers and endowed with brick based interface properties (as suggested in [19]), is almost negligible.
- If the cohesive law is applied on both bricks and mortar layers, with different interface properties, calibrated trough Eq. (1) on the basis of the bulk material parameters (green dashed dot line), a larger maximum load is achieved, which can be easily explained in view of the higher mortar material properties.

It was also observed, with reference to 150 mm reinforcement length, that both the experimental and numerical response, the latter being achieved with two different interface parameters sets (one for the brick–FRP and one for the mortar joint–FRP interface, respectively), was characterized by two peaks. The first peak was obtained when the crack front reached the second clay brick, see Fig. 14 (point A). After the following load drop characterized by a snap-back branch down to point B, a load recovery occurred when the debonding process reached the second mortar layer (point C), due to its enhanced strength and toughness properties. A best fitting procedure was then applied to the mortar interface properties only (resulted in the following calibration: $\tau_f = 5.84$ MPa and $\Gamma_{Fm} = 0.58$ N/mm) and the curve obtained (green continuous line, see Figs. 12 and 13) well agreed with the experimental one.

7. Conclusions

Debonding phenomena between a carbon fiber reinforced polymer strip and a masonry substrate were investigated by means of single-lap shear specimens with different bond lengths. To monitor the complete failure process, the tests were conducted with a clip gauge located at the free end of the strip as feedback signal to the servo-controller. It was not clearly detected in the experiments the formation of a resistant bulb inside the bulk material at the end of the reinforcement, as well as was emerged on concrete specimens [25].

The numerical results show that, by means of the cohesive approach implemented, it was possible to follow the overall response of the specimens, even with snap-back softening branch in the post failure range, which represents a remarkable result rarely achieved in the literature. Indeed the numerical predictions turn out to be very close to the experimental findings both in the pre and post-peak parts of the load–displacement curve.

The experimental results showed some similarities with the results on concrete specimens, but also some differences in relation to the damage processes and the consequent failure mechanisms. The numerical simulations and the experimental results showed that the debonding process was dominated by mode-II cracking, but at the end of the reinforcement a germinal mix-mode cracking arose. This confirmed the presence of two potential different competing failure processes even in the case of masonry specimens. The difference with respect to concrete specimens, where the presence of the bulb mechanism is more evident, may be explained in view of the different microstructure of the two materials and the consequent different progressive damage and cracking mechanisms occurring. Indeed, while concrete fracture is characterized by diffuse microcracking, the considered brick clay is characterized by significant brittleness and spalling (exfoliation), occurring with respect to preferential planes.

The adopted finite element model, based on a proper cohesive law and on the Riks procedure to follow also snap-back behavior, was validated on the basis the experimental results. It was confirmed numerically and experimentally the influence of the effective bond length on the ultimate load. In particular:

- If the effective bond length is lower than the minimum bond length, the ultimate load increases with the bond length and the ultimate load depends on both fracture energy Γ_F and interface shear strength τ_f.
- If the effective bond length is equal or higher than the minimum bond length, the ultimate load is no longer affected by the bond length and it depends only on Γ_F.

Finally, additional numerical cases were considered in order to better understand the role played by the interface modeling approach on the overall response of the system. These analyses were able to explain the system response emerged in relation to the longest reinforcement length, which was characterized by two load peaks, occurred, as explained by the numerical analyses, in view of the specimen heterogeneity due to the higher mechanical properties of the mortar layer.

References

[1] Nakaba M, Kanakubo T, Furuta T, Yoshizawa H. Bond behavior between fiber-reinforced polymer laminates and concrete. ACI Struct J 2001;98(3):359–67.

[2] Monti G, Nisticò N. Square and rectangular concrete columns confined by CFRP: experimental and numerical investigation. Mech Compos Mater 2008;44(3):289–308.

[3] Ascione L, Berardi VP, Feo L, Mancusi G. A numerical evaluation of the interlaminar stress state in externally FRP plated RC beams. Compos Part B: Eng 2005;36(1):83–90.

[4] Lu XZ, Teng JG, Ye LP, Jiang JJ. Bond–slip models for FRP sheets/plates bonded to concrete. Eng Struct 2005;27(6):920–37.

[5] Ferracuti B, Savoia M, Mazzotti C. Interface law for FRP–concrete delamination. Compos Struct 2007;80(4):523–31.

[6] Pisani MA. Evaluation of bending strength of RC beams strengthened with FRP sheets. ASCE J Compos Constr 2006;10(4):313–20.

[7] Ascione L, Feo L, Fraternali F. Load carrying capacity of 2D FRP/strengthened masonry structures. Compos Part B: Eng 2005;36(8):619–26.

[8] Aiello MA, Sciolti SM. Analysis of masonry structures strengthened with CFRP sheets. Constr Build Mater 2006;20(1):90–100.

[9] Aiello MA, Sciolti SM. Analysis of the durability of the bond between masonry and FRP sheets. In: Proceedings of 8th international symposium on FRP reinforcement for concrete structures, Patras, GR; 2007.

[10] Panizza M, Garbin E, Valluzzi MR, Modena C. Bond behavior of CFRP and GFRP laminates on brick masonry. In: Proceedings of 6th international conference on structural analysis of historical constructions, Bath, UK; 2008.

[11] Fedele R, Milani G. A numerical insight into the response of masonry reinforced by FRP strips. The case of perfect adhesion. Compos Struct 2010;92(10):2345–57.

[12] Grande E, Imbimbo M, Sacco E. Simple model for bond behavior of masonry elements strengthened with FRP. J Compos Constr 2010;15(3):354–63.

[13] Grande E, Imbimbo M, Sacco E. Bond behaviour of CFRP laminates glued on clay bricks: experimental and numerical study. Compos Part B: Eng 2011;42(2):330–40.

[14] Ghiassi B, Marcari G, Oliveira DV, Lourenço PB. Numerical analysis of the bond behavior between masonry bricks and composite materials. Eng Struct 2012;43:210–20.

[15] Foraboschi P, Vanin A. New methods for bonding FRP strips onto masonry structures: experimental results and analytical evaluations. Compos: Mech, Comput, Appl 2013;4(1):1–23.

[16] Ceroni F, Garofano A, Pecce M. Modelling of the bond behavior of tuff elements externally bonded with FRP sheets. Compos Part B: Eng 2014;59:248–59.

[17] Carozzi FG, Milani G, Poggi C. Mechanical properties and numerical modeling of fabric reinforced cementitious matrix (FRCM) systems for strengthening of masonry structures. Compos Struct 2014;107:711–25.

[18] Foraboschi P. Church of San Giuliano di Puglia: seismic repair and upgrading. Eng Fail Anal 2013;33:281–314.

[19] CNR DT200. Istruzioni per la progettazione, l'esecuzione ed il controllo di interventi di consolidamento statico mediante l'utilizzo di compositi fibrorinforzati; 2013.

[20] Massart TJ, Peerlings RHJ, Geers MGD. An enhanced multi-scale approach for masonry wall computations with localization of damage. Int J Numer Methods Eng 2007;69:1022–59.

[21] Ghiassi B, Oliveira DV, Lourenço PB, Marcari G. Numerical study of the role of mortar joints in the bond behavior of FRP–strengthened masonry. Composites: Part B 2013;46:21–30.

[22] UNI EN 772-1. Methods of test for masonry units Part 1: determination of compressive strength, June; 2011.

[23] UNI EN 1015-11. Methods of test for mortar for masonry Part 11: determination of flexural and compressive strength of hardened mortar, March; 2007.

[24] Biolzi L, Labuz JF. Global instability and bifurcation in beams composed of rock-like materials. Int J Solids Struct 1993;30(3):359–70.

[25] Biolzi L, Ghittoni C, Fedele R, Rosati G. Experimental and theoretical issues in FRP–concrete bonding. Constr Build Mater 2013;41:182–90.

[26] Bocciarelli M, Colombi P, Fava G, Poggi C. Interaction of interface delamination and plasticity in tensile steel members reinforced by CFRP plates. Int J Fract 2007;146(1–2):79–92.

[27] Bocciarelli M, Colombi P. Elasto-plastic debonding strength of tensile steel/CFRP joints. Eng Fract Mech 2012;85:59–72.

[28] Ortiz M, Pandolfi A. Finite-deformation irreversible cohesive elements for three-dimensional crack-propagation analysis. Int J Numer Methods Eng 1999;44(9):1267–82.